# Structural and thermodynamic properties of compressed palladium: *Ab initio* and molecular dynamics study

Zhong-Li Liu* and Jie-Hui Yang
*College of Physics and Electric Information, Luoyang Normal University, Luoyang 471022, China*

Ling-Cang Cai and Fu-Qian Jing
*Laboratory for Shock Wave and Detonation Physics Research, Institute of Fluid Physics, P.O. Box 919-102, Mianyang 621900, Sichuan, China*

Dario Alfè
*Department of Earth Sciences and Department of Physics and Astronomy, Thomas Young Centre at UCL, and London Centre for Nanotechnology, UCL, Gower Street, London WC1E 6BT, United Kingdom*
(Received 20 October 2010; published 26 April 2011)

First-principles and classical molecular dynamics simulations have been performed to study the structural and thermodynamic properties of Pd under pressure. By comparing the Gibbs free energy, in the quasiharmonic approximation (QHA), of the face-centered cubic (fcc) phase with those of the hexagonal-close-packed (hcp) and body-centered-cubic (bcc) phases we found that the fcc phase is stable up to 500 GPa and 5000 K. The predicted high-temperature elastic constants of fcc Pd agree well with experiments. The phonon dispersion curves are obtained at various pressures. In contrast with experiments we did not observe any phonon anomalies in Pd. We reproduced the thermodynamic properties of Pd accurately by taking into account the electron and phonon contributions to the free energy of Pd. The obtained thermal expansion coefficient, Hugoniot curves, and specific heat capacity compare well with experiments. In particular, the excellent agreement of the thermal expansion coefficients with experiment supports the validity of the QHA for Pd at high temperatures. Our QHA-based Hugoniot curves also show good agreement with experiments and our dynamic shock simulations. Shocks along [100] produced a melting temperature with a superheating of 18.3% at 226 GPa, compared with our high-pressure melting curve of Pd from coexistence-phase simulations based on an embedded atom model.

DOI: 10.1103/PhysRevB.83.144113 PACS number(s): 05.70.−a, 65.40.−b, 62.20.−x, 74.10.+v

## I. INTRODUCTION

Palladium has a wide range of applications in jewelery, dentistry, metalizing ceramics, catalysis, hydrogen storage, and so on. Recently, it has attracted an increasing interest from researchers due to its fascinating features both in nanoscale and bulk systems.[1–3] In the nanoscale field, recent interest in hydrogen storage systems and nanoscale devices fully highlighted the key role that palladium plays.[3] For bulk systems, in high-pressure experiments Pd is commonly used as a pressure standard because of its unique face-centered-cubic (fcc) structure under high pressure, and its equation of state (EOS) has been investigated experimentally.[4–7]

Although superconductivity in bulk Pd has not yet been observed experimentally, Pd film irradiated by $He^+$ ions can be transformed into a superconductor, with the highest superconducting transition temperature ($T_c$) of 3.2 K.[8,9] Recently, using the full-potential linear muffin-tin orbital (FP-LMTO) method Takezawa *et al.*[10] reported a $T_c$ value of 0.514 K at ambient pressure for bulk Pd when the spin fluctuation effect of the electrons are not considered. They suggested that Pd also has the potential to be a superconductor under high pressure where the spin fluctuation effect becomes less important, and superconductivity appears.[10] Most recently, a large spin Hall conductivity (SHC) of Pd at low temperature was predicted by first-principles band structure calculations, and as temperature increases, the SHC in Pd decreases monotonically.[11]

First-principles calculations show that there exists an anomalously large broadening for the transverse phonon mode $T_1$ in the $\Sigma$ direction and this mode contributes most strongly to the electron-phonon scattering processes on the Fermi surface,[12] consistent with experimental observations.[13,14] In addition, the experimentally[13,15,16] observed Kohn anomaly[17] along [110] in Pd was also reproduced using density functional perturbation theory (DFPT),[18,19] and paramagnons were found to play no significant role in the [110] phonon dispersion.[3] However, others[10,20] observed no phonon anomalies in *ab initio* studies.

Theoretical studies of the thermal EOS are complementary to experiments and are particularly useful for extending the domain to regions of phase space that cannot be reached experimentally. The elastic properties of materials at high pressures are also of key importance for us to understand their underlying static and dynamic responses to pressure, mechanical strength, and the EOS. Experimental studies of the elastic constants of Pd are limited to ambient pressure[21,22] or very low pressure (below 1 GPa).[23] Furthermore, so far no systematic investigations of the thermal EOS of Pd have been reported. These are the main motivations for the present work.

Here we apply DFPT[18,19] and classical molecular dynamics to perform a series of detailed simulations on a wide range of properties for Pd, including elastic, lattice dynamic, and thermodynamic properties. First, we examine the phase transition of Pd at high pressure, according to Gibbs free energy differences of several possible structures after determining the phonon dispersions of different phases at high pressures. Then, based on phonon frequencies, we deduce the thermodynamic

 

properties of fcc Pd within the framework of the quasiharmonic approximation (QHA).

The rest of the paper is organized as follows. In Sec. II, we describe the details of the calculations. In Sec. III, we present the results of the lattice dynamics, elastic, and thermodynamic properties. Finally, Sec. IV presents a discussion and conclusions.

## II. COMPUTATIONAL DETAILS

In the framework of the QHA, the Helmholtz free energy of a metal system is written as

$$F(V,T) = E_{\text{static}}(V) + F_{\text{el}}(V,T) + F_{\text{zp}}(V,T) + F_{\text{ph}}(V,T), \tag{1}$$

where $E_{\text{static}}(V)$ is the first-principles zero-temperature energy of a static lattice at volume $V$ and $F_{\text{el}}(V,T)$ is the electronic free energy arising from the electronic thermal excitations at temperature $T$ and volume $V$. $F_{\text{el}}(V,T)$ can be evaluated via the standard methods of finite-temperature DFT developed by Mermin (the Fermi-Dirac distribution):[24]

$$F_{\text{el}}(V,T) = E_{\text{el}}(V,T) - TS_{\text{el}}(V,T). \tag{2}$$

The electronic energy due to the electronic excitations is given by

$$E_{\text{el}}(V,T) = \int n(\epsilon) f(\epsilon) \epsilon d\epsilon - \int^{\epsilon_F} n(\epsilon)\epsilon d\epsilon, \tag{3}$$

where $n(\epsilon)$ is the electronic density of states (EDOS) at the energy eigenvalues $\epsilon$, $f$ is the Fermi distribution function, and $\epsilon_F$ is the energy at the Fermi level.

The electronic entropy is calculated by

$$S_{\text{el}}(V,T) = -2k_B \sum f_i \ln f_i + (1-f_i)\ln(1-f_i), \tag{4}$$

where $k_B$ is Boltzmann's constant.

The term $F_{\text{zp}}$ in Eq. (1) is the zero-point motion energy of the lattice given by

$$F_{\text{zp}} = \frac{1}{2}\sum_{\mathbf{q},j} \hbar\omega_j(\mathbf{q},V), \tag{5}$$

where $\omega_j(\mathbf{q},V)$ is the phonon frequency of the $j$th mode of wave vector $\mathbf{q}$ in the first Brillouin zone (BZ).

The last term in Eq. (1) is the phonon free energy due to lattice vibrations, and it can be obtained from

$$F_{\text{ph}}(V,T) = k_B T \sum_{\mathbf{q},j} \ln\{1 - \exp[-\hbar\omega_j(\mathbf{q},V)/k_B T]\}. \tag{6}$$

Within the QHA, the phonon frequencies depend on temperature slightly due to electronic excitations for transition metals, but we neglected this dependence.

We determined the vibrational frequencies of Pd using DFPT,[18,19] as implemented in the QUANTUM-ESPRESSO package.[25] For the exchange-correlation functional we have taken the Perdew Zunger local-density approximation (LDA)[26] and used an ultrasoft pseudopotential.[27] We have also performed the phonon calculations using the generalized gradient approximation (GGA) proposed by Perdew, Burke, and Ernzerhof (PBE)[28] and found a worse agreement of the phonon dispersions of fcc Pd with experiments, just like others' previous conclusions with the GGA;[3,10] therefore all the calculated results are only based on the LDA. A nonlinear core correction to the exchange-correlation energy function was introduced to generate a Vanderbilt ultrasoft pseudopotential for Pd with the valence electrons configuration $4d^9 5s^1$, and the ultrasoft pseudopotentials were generated with a scalar-relativistic calculation.

Careful tests on $\mathbf{k}$ and $\mathbf{q}$ grids, the kinetic energy cutoff, and other technical parameters were performed to guarantee convergence of phonon frequencies and free energies. For fcc Pd, we computed the dynamical matrices using an $8 \times 8 \times 8$ q grid, giving 29 wave vectors $\mathbf{q}$ in the irreducible wedge of the first BZ. The kinetic energy cutoff, the energy cutoff for the electron density, and the $\mathbf{k}$ grids were chosen to be 60 Ry, 500 Ry, and $24 \times 24 \times 24$ Monkhorst-Pack (MP)[29] meshes in both total energy and phonon dispersion calculations, respectively. We computed the dynamical matrices at 29 wave ($\mathbf{q}$) vectors using the $8 \times 8 \times 8$ $\mathbf{q}$ grid for body-centered cubic (bcc) structures and 10 wave ($\mathbf{q}$) vectors using the $5 \times 5 \times 3$ $\mathbf{q}$ grid for hexagonal-close-packed (hcp) structures in the irreducible wedge of the first BZ, and the full phonon dispersion was obtained through Fourier interpolation. We applied a Fermi-Dirac smearing width of 0.032 Ry.

The geometric mean phonon frequency $\bar{\omega}$ is defined by

$$\ln\bar{\omega} = \frac{1}{N_{\mathbf{q}j}}\sum_{\mathbf{q}j} \ln\omega_{\mathbf{q}j}, \tag{7}$$

where $\omega_{\mathbf{q}j}$ is the phonon frequency of the branch $j$ at the wave vector $\mathbf{q}$ and $N_{\mathbf{q}j}$ is the number of branches times the total number of $q$ points in the sum. For all volumes, the geometric mean phonon frequency $\omega$ was converged to 1 $\text{cm}^{-1}$ with respect to the $\mathbf{k}$ mesh and kinetic energy cutoff was used.

## III. RESULTS

### A. Structural and elastic properties

Experiment and *ab initio* calculations indicated that Pd has an fcc structure at least up to 77.4 GPa[5] and 500 GPa,[30] respectively. We also performed detailed calculations to verify this. First, we calculated the zero-temperature energies of the bcc, fcc, and hcp structures in the pressure range of 0–1000 GPa. For the hcp structure, the volume and the ratio between the hexagonal $c$ axis and $a$ axis ($c/a$) were optimized using the variable cell relax[31] method for each pressure and found to be around 1.64 and only weakly dependent on pressure. The accuracy of the target pressure for all calculations is better than 1 kbar. The optimized $a$ and $c$ are plotted in the inset of Fig. 1. Second, we calculated the enthalpies $H = E + PV$ as a function of pressure for the three structures. Then the enthalpy differences relative to the fcc structure were deduced for all pressures between 0 and 1000 GPa (Fig. 1). The enthalpy differences are positive and the fcc phase remains stable up to at least 1000 GPa, consistent with experiments[5] and other *ab initio* results.[30]

We also calculated the phonon dispersion curves of bcc and hcp phases to further test the stability of the fcc phase at high temperature and high pressure. The phonon dispersion curves of bcc and hcp structures are presented in Fig. 2. One of the three acoustical modes of the bcc phase along the

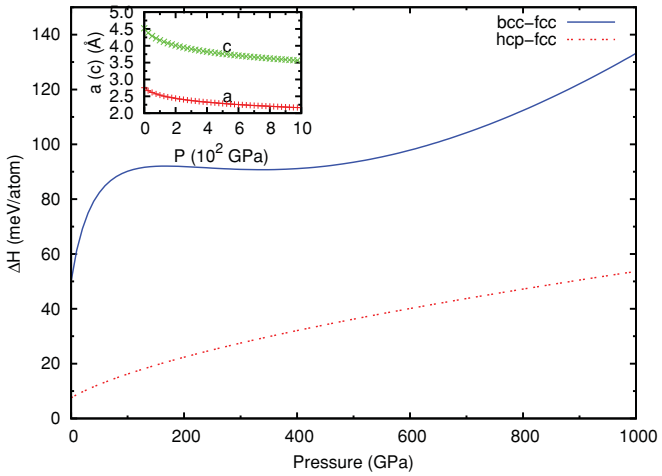


FIG. 1. (Color online) Enthalpy differences $\Delta H$ of the bcc and hcp structures with respect to fcc in Pd as a function of pressure.

Γ-$N$ direction shows imaginary frequencies up to 800 GPa, indicating the instability of bcc in the whole pressure range of interest (in the framework of QHA). We did not find soft modes for hcp, and the obtained phonon dispersion curves show good

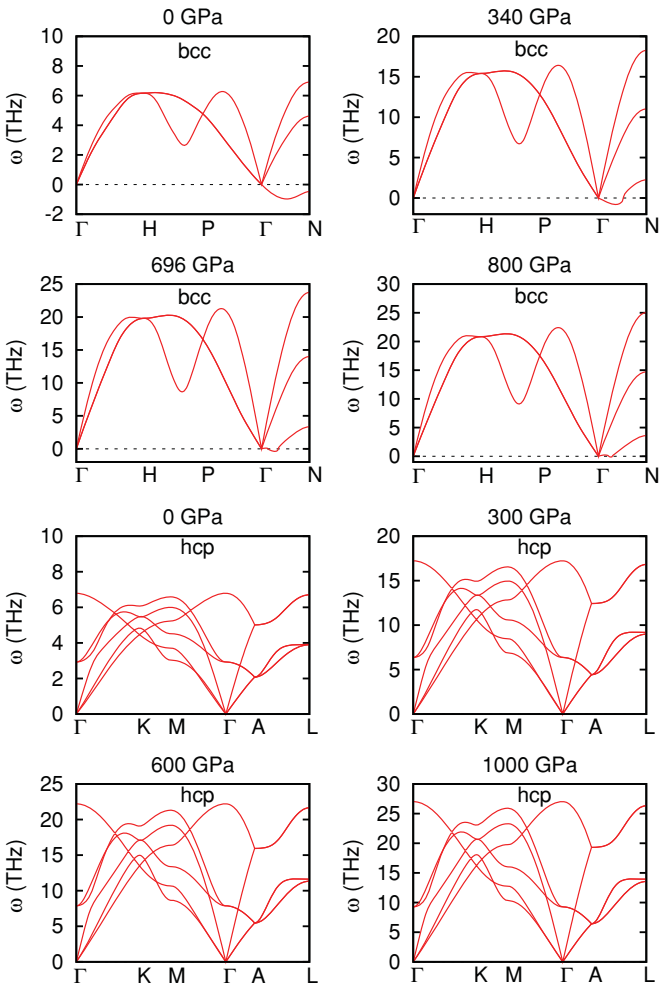


FIG. 2. (Color online) The phonon dispersion curves of bcc and hcp Pd at different pressures.

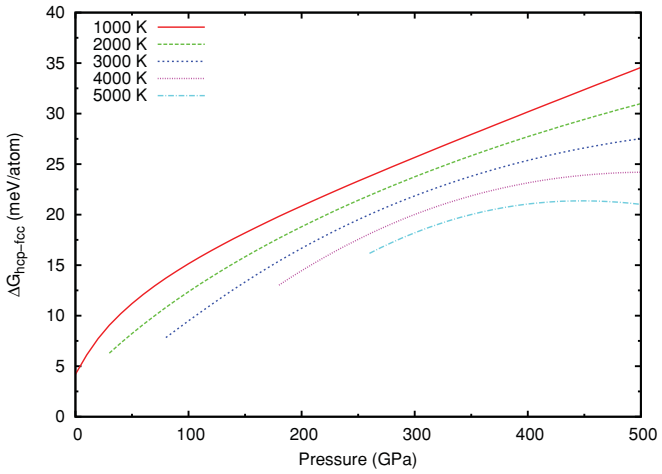


FIG. 3. Gibbs free energy differences $\Delta G$ of the hcp structure with respect to fcc in Pd as a function of pressure at different temperatures.

stability up to 1000 GPa. The Gibbs free energy $G = F + PV$ of the hcp and fcc phases as the function of temperature at different pressures are derived from the phonon frequencies calculated using the $30 \times 30 \times 30$ Monkhorst-Pack **k** mesh. The Gibbs free energy differences between hcp and fcc is plotted in Fig. 3 (in which data beyond the melting temperature are not displayed; see below). We do not find any crossings of the Gibbs free energy curves at pressures below 500 GPa, which implies that within the QHA fcc is more stable than hcp in the range of pressure and temperature investigated. For this reason, all calculations were performed for the fcc phase. Of course, we recognize that anharmonic effects could still change the relative stability of the structures investigated, but a detailed study of anharmonic effects goes beyond the scope of the present work.

A cubic lattice system has three independent elastic constants, $C_{11}$, $C_{12}$, and $C_{44}$; the relationship between the elastic constants and the bulk modulus can be written as

$$B = \frac{C_{11} + 2C_{12}}{3}. \tag{8}$$

To determine $C_{11}$ and $C_{12}$, we applied the following volume-conserving strain matrix:

$$\epsilon = \begin{pmatrix} \delta & 0 & 0 \\ 0 & \delta & 0 \\ 0 & 0 & (1+\delta)^{-2} - 1 \end{pmatrix}, \tag{9}$$

where $\delta$ is the infinitesimal strain magnitude. Then the strain energy is written as a function of the strain,

$$E(\delta) = E(0) + 3(C_{11} - C_{12})V\delta^2 + O(\delta^3), \tag{10}$$

where $E(0)$ is the energy of the unstrained unit cell and $V$ is the corresponding volume. Combining this result with Eq. (8), we derived $C_{11}$ and $C_{12}$ by fitting the third-order polynomial curves to the $E$-$\delta$ data and finding the quadratic coefficients. $C_{44}$ is deduced by applying the following volume-conserving

strain matrix to the unit cell:

$$\epsilon = \begin{pmatrix} 0 & \delta & 0 \\ \delta & 0 & 0 \\ 0 & 0 & (1-\delta^2)^{-1} - 1 \end{pmatrix}, \quad (11)$$

and correspondingly the strain energy is

$$E(\delta) = E(0) + 2C_{44}V\delta^2 + O(\delta^4). \quad (12)$$

Similarly, $C_{44}$ is calculated by finding the quadratic coefficients.

To calculate the elastic constants accurately, we used the $40 \times 40 \times 40$ Monkhorst-Pack[29] **k** mesh in self-consistent calculations. The high-pressure (HP) elastic constants and high-temperature (HT) elastic constants of Pd are both obtained by using the method described above. For HP elastic constants, we first derived the volume as a function of pressure by fitting a fourth-order finite-strain EOS[33,34] to the calculated energy-volume data. Then we calculated the elastic constants at each volume. For the HT elastic constants we should use energy-stress data obtained at high temperature. These could be calculated in a molecular dynamic simulation (if the temperature is large enough to neglect nuclear quantum effects), or by using the QHA free energies (if the temperature is low enough so that anharmonic effects are negligible). However, the largest effect of temperature is that of making the crystal expand; therefore we have decided to ignore the fine details of the dependence of the stresses with temperature and assumed that they only depend on temperature through the dependence on temperature of the volume.[35,36] This approximation only introduced small errors for the elastic constants of the cubic systems.[35] As expected the calculated HT elastic constants are in very good agreement with experiments.[35] We first extrapolated the volume as a function of temperature by fitting a fourth-order finite-strain EOS[33,34] to the calculated free energy versus volume data within the QHA (see Sec. III B). Then we evaluated the elastic constants at each volume using the same method for HP.

The calculated HP and HT elastic constants of Pd are shown in Table I and Fig. 4, respectively. From Table I, one notes that $C_{44}$ agrees very well with experiment. However, $C_{11}$ is overestimated by 17.1% and $C_{12}$ is underestimated by 16.9%, compared with experiment. The three elastic constants

TABLE I. The calculated 0 K elastic constants of fcc Pd under high pressure. $P$, $C_{ij}$, and $B$ are in GPa. The experimental (Ref. 21) elastic constants at 4.2 K and 1 atm are also listed.

| $P$ | $V$ (Å$^3$) | $C_{11}$ | $C_{12}$ | $C_{44}$ | $B$ |
|---|---|---|---|---|---|
| 0.01 | 14.8305 | 274.3 | 146.3 | 71.6 | 189.0 |
| 49.9 | 12.6613 | 564.2 | 311.5 | 134.5 | 395.7 |
| 103.6 | 11.5104 | 824.5 | 459.5 | 189.2 | 581.2 |
| 153.3 | 10.8056 | 1043.1 | 583.7 | 234.7 | 736.8 |
| 204.2 | 10.2641 | 1253.0 | 702.6 | 277.7 | 886.1 |
| 253.9 | 9.8430 | 1447.9 | 813.1 | 317.1 | 1024.7 |
| 304.1 | 9.4906 | 1636.9 | 920.0 | 355.4 | 1159.0 |
| 356.1 | 9.1812 | 1825.6 | 1026.7 | 392.9 | 1293.0 |
| 406.1 | 8.9234 | 2001.8 | 1126.1 | 427.9 | 1418.0 |
| Expt. [ 21] | 14.5104 | 234.1 | 176.1 | 71.2 | 195.5 |

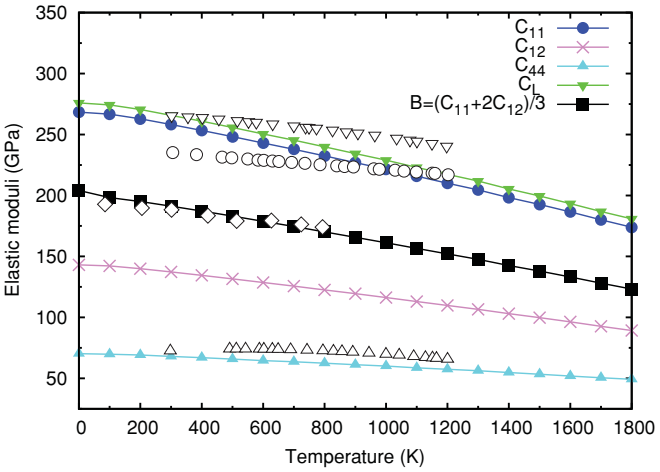


FIG. 4. (Color online) The calculated elastic moduli as a function of temperature [$C_L = (C_{11} + C_{12} + 2C_{44})/2$]. The experimental data (Ref. 22) are also shown for comparison: open circles, $C_{11}$; triangles up, $C_{44}$; triangles down, $C_L$. The open diamonds are experimental data of $B_T$ from Ref. 32.

increase as pressure increases and decrease with increasing temperature linearly. The HT elastic constants and their general trend are also in good agreement with experiment[22] (Fig. 4). The temperature variation of $C_{44}$ agrees well with experiment, despite a small underestimation. The bulk moduli at high temperature are also in good agreement with the experimental data, whereas the trends of $C_{11}$ and $C_L$ diverge from experiment slightly, possibly due to the exchange-correlation functional employed. Nevertheless, the general trends of the elastic moduli with temperature are very similar to the recent *ab initio* results of Al, Cu, Ni, Mo, and Ta.[35] This appears to indicate that our approximation for calculating elastic constants at HT, based on the neglect of the detailed behavior of the stress at high temperature, is reasonable.

### B. Phonon and thermodynamic properties

Within the DFPT, a unit cell is used for calculating the phonon dispersion curves. Figure 5 shows the obtained dispersion curves at zero pressure along several high-symmetry

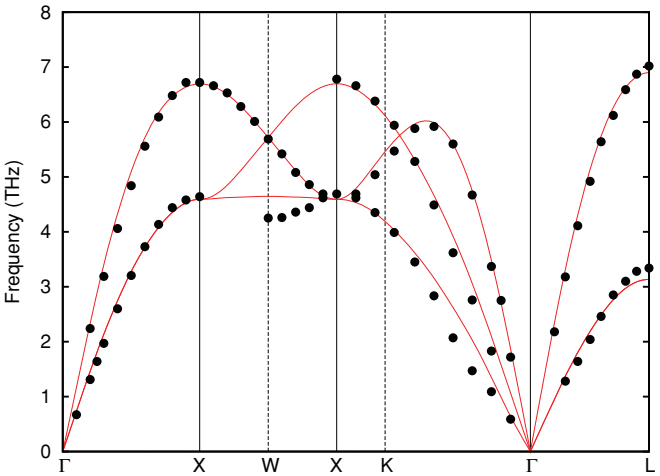


FIG. 5. (Color online) Phonon dispersion curves of Pd at 0 GPa. The solid circles are the neutron diffraction data (Ref. 15).

directions in the first BZ for both transverse acoustical (TA) and longitudinal acoustical (LA) branches. We note that the agreement of the dispersion curves with experiment[15] is generally good, apart from the lowest acoustic branch in the $\Gamma$-$K$ (also observed in Ref. 3) and $W$-$X$ directions. This possibly can be attributed to the LDA exchange-correlation functional and the ultrasoft pseudopotential used. Fortunately, the small phonon deviations almost do not affect the calculations of the thermodynamic properties. We repeated the phonon calculations for another 15 different volumes, and from all the phonon dispersion relations we obtained the phonon free energies according to Eq. (1).

Miiller and Brockhouse observed the phonon anomalies along the [110] direction in the first BZ of Pd in their inelastic neutron scattering experiments.[13,15,16] Savrasov and Savrasov[20] and Takezawa *et al.*[10] indicated that they did not find any phonon anomalies in Pd using the FP-LMTO method.[37] More recently, Stewart[3] reported the anomalies in Pd using DFPT and the pseudopotential approach as implemented in the QUANTUM-ESPRESSO package.[25] We reproduced the phonon anomalies found by Stewart using his very same parameters: MP **k** mesh ($16 \times 16 \times 16$), plane wave energy cutoff (34 Ry), smearing function (Methfessel-Paxon), and size of smearing (0.01 Ry). However, when we use our own choice of parameters—MP **k** mesh ($24 \times 24 \times 24$), plane wave energy cutoff (60 Ry), smearing function (Fermi-Dirac), and size of smearing (0.032, 0.01 Ry, and smaller values)—we do not find such phonon anomalies.

We derived the Helmholtz free energy as a function of volume $V$ and temperature $T$ from Eq. (1) after taking into account the thermal electronic excitation and phonon contributions. In order to deduce the thermodynamic properties, we fitted a fourth-order finite-strain EOS to the calculated free energy versus volume data at each temperature. The fitted 300 K thermal EOS parameters and the isothermal compressional curves are compared with experiments in Table II and Fig. 6, respectively, and they show good agreement.

The thermal expansion coefficient is often used to check the accuracy of the thermal properties from first-principles calculations. The volume thermal expansion coefficient $\alpha_V$ can be calculated by

$$\alpha_V = \frac{1}{V}\left(\frac{\partial V}{\partial T}\right)_P. \tag{13}$$

Figure 7 shows the thermal expansion coefficient as a function of temperature at different pressures. Our zero-pressure results are in excellent agreement with experimental data[38] in the low-temperature region, while when the temperature is above 800 K (about half the melting point of 1828 K[41]) the zero-pressure thermal expansion coefficient gradually deviates from experiment. This is the result of the neglect of anharmonicity

TABLE II. The fitted 300 K EOS parameters compared with the experimental data (Ref. 21).

| | $V_0$ (Å$^3$) | $B_0$ (GPa) | $B_0'$ |
|---|---|---|---|
| Present | 14.8305 | 189 | 5.23 |
| Expt. | 14.6231 | 193 | — |

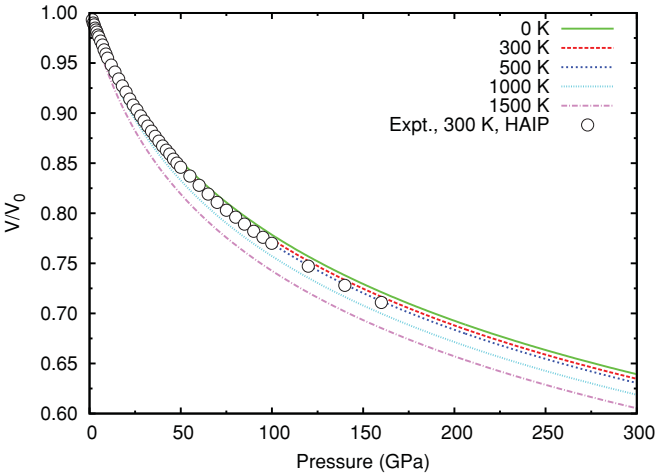


FIG. 6. (Color online) The isothermal compressional curves at different temperatures. The experimental data are from Ref. 21.

caused by phonon-phonon interactions. This behavior is also found in other transition metals, such as Ta[42] and Pt.[43] Generally, when temperature is below half the melting point the QHA is accurate enough, while full anharmonicity effects must be taken into account in the high-temperature region.[42]

The linear thermal expansivity was also obtained using $(a - a_0)/a_0$, where $a_0$ is the lattice constant at 0 K. In Fig. 8, we plot the lattice constant and $(a - a_0)/a_0$ as a function of temperature. Although one finds the systematic deviation of our lattice constants from experiments, the deviation is within the reasonable error of density functional theory (DFT) (less than 1%). Thus the lattice constant and the linear thermal expansivity are both in excellent agreement with experiments.[39,40]

The Hugoniot curve is one of the fundamental properties of materials; it reflects the response of the material to both pressure and temperature simultaneously. We calculated the

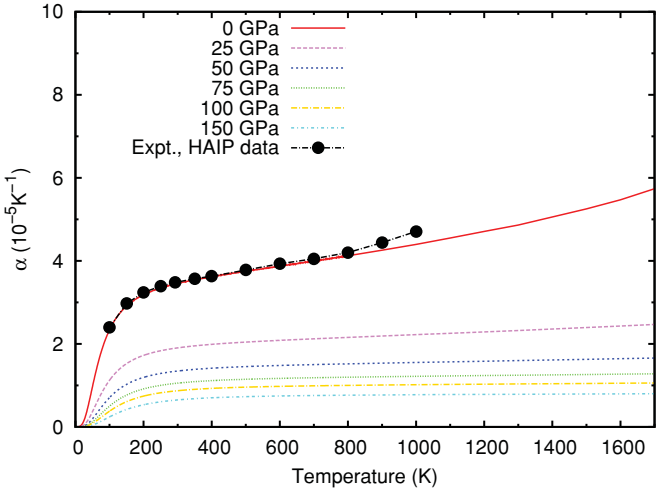


FIG. 7. (Color online) The thermal expansion coefficient as a function of temperature at different pressures. Our zero-pressure results are in excellent agreement with the experimental data (Ref. 38).

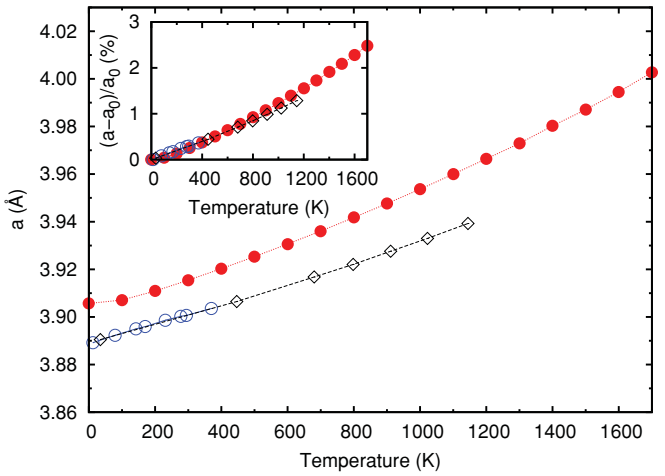


FIG. 8. (Color online) The lattice constant and the linear thermal expansivity (inset) as a function of temperature (red solid circles). The experimental data are from Refs. 39 (open diamonds) and 40 (blue open circles).

Hugoniot $P$-$V$ and $P$-$T$ curves according to the Rankine-Hugoniot formula

$$U_H - U_0 = \tfrac{1}{2}(P_H + P_0)(V_0 - V_H), \tag{14}$$

where $U_H$, $P_H$, and $V_H$ are the molar internal energy, pressure, and volume along the Hugoniot states, respectively, and $U_0$ and $V_0$ are the molar internal energy and volume at pressure $P_0$ and room temperature. Although our theoretical results deviate slightly from experiments[4,44–46] above 150 GPa (Fig. 9), the agreement of our $P$-$V$ curve with experiments is reasonably good in the whole pressure range of interest (Fig. 9).

In order to check our calculated Hugoniot $P$-$T$ curve, we also performed classical molecular dynamics (MD) simulations to derive the shock behavior of Pd using the embedded-atom-method (EAM) potential.[47] Within the EAM formalism the total potential energy $E_{\rm tot}$ of a metal system containing $N$ equal atoms can be written as a sum of the embedding energy $F$ and a pair potential $\phi$:[48]

$$E_{\rm tot} = \sum_i^N F_i(\rho_i) + \frac{1}{2}\sum_i^N \sum_{j<i}^N \phi(r_{ij}), \tag{15}$$

where $r_{ij}$ is the distance between the atoms $i$ and $j$. The function $F_i(\rho_i)$ is the energy needed to embed the atom $i$ into the background electron density $\rho_i$, which is the superposition of the atomic densities,

$$\rho_i = \sum_{i\neq j}^N \rho_j(r_{ij}). \tag{16}$$

For the specific form of the functions and their parameters, see Ref. 48.

The details of the shock-wave simulations can be found in our previous work.[49] All the MD simulations were conducted with the LAMMPS[50–52] molecular dynamics code. For the shock simulation, we used $\sim 2.5 \times 10^5$ Pd atoms in the fcc structure. Loading with various piston velocities along the three typical orientations [100], [110], and [111], we deduced the shock $u_s$-$u_p$ relations for the three orientations according to the Hugoniot jump condition

$$p_{xx} = \rho_0 u_s u_p, \tag{17}$$

where $p_{xx}$ is the stress along the loading direction and $\rho_0$ is the initial density of single-crystal Pd. It should be noted that Eq. (17) is only valid for the jump condition. The obtained $u_s$-$u_p$ relation along the [100] direction is compared with the experiments[4,44–46] in Fig. 10. The $u_s$-$u_p$ relation of the [100] orientation loading is very close to the polycrystalline experiment because of the preferred [100] orientation in annealed polycrystalline metals.[49]

The Hugoniot $P$-$T$ curve (Fig. 11) from the shock simulations greatly supports the results from the QHA, while the Hugoniot $P$-$V$ curve deviates from it slightly. The high-pressure melting curves of Pd are also calculated using the two-phase coexistence simulations, and the system contained 8000 Pd atoms in the fcc structure. The details of the coexistence-phase simulations are described in our previous

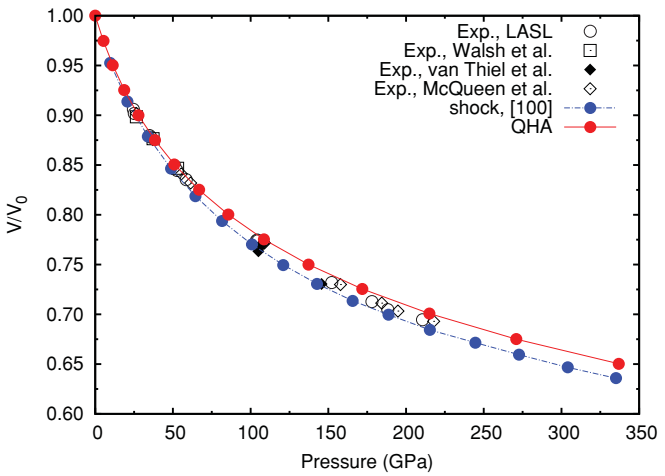


FIG. 9. (Color online) The Hugoniot $P$-$V$ curve compared with the shock experimental data (Refs. 4,44–46).

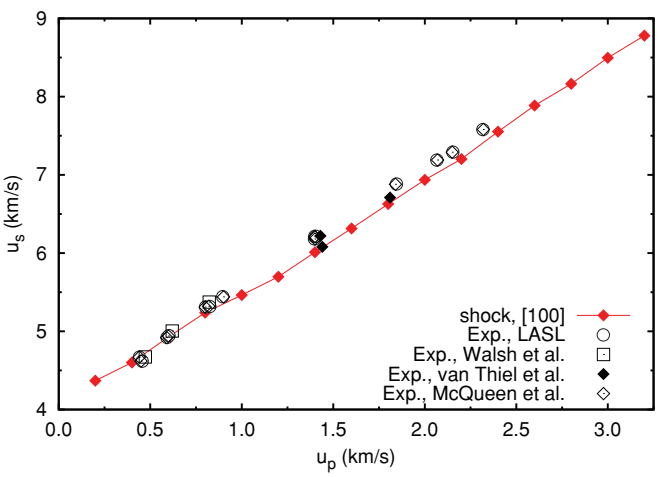


FIG. 10. (Color online) $u_s$-$u_p$ relation along the [100] directions in comparison with experiments (Refs. 4,44–46).

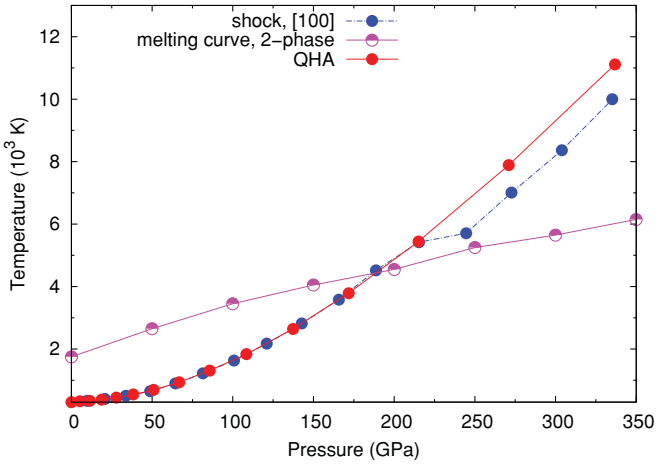


FIG. 11. (Color online) The Hugoniot $P$-$T$ curve from QHA in comparison with the results of shock simulations along [100]. The high-pressure melting curve of Pd from the coexistence-phase simulations is also displayed.

work.[49,53] The obtained melting point of Pd at 0 GPa is 1750 K, consistent with the experimental value of 1828 K.[41] Shocks along [100] (5855 K at 226 GPa) lead to the superheating of 18.3%, compared with our coexistence-phase results (4782 K at 226 GPa). This is similar to the shock melting behavior of Pt, which has a superheating of 18% at 280 GPa.[49] Unfortunately, there are no high-pressure experimental data to check our melting curve of Pd under high pressure.

The specific heat at constant volume is defined by

$$C_V = \left(\frac{\partial U}{\partial T}\right)_V, \tag{18}$$

where $U$ is the internal energy of the system. The thermal expansion caused by anharmonic effects results in a difference between $C_P$ and $C_V$. The difference between $C_P$ and $C_V$ can be written as

$$C_P - C_V = \alpha_V^2(T) B_0 V T, \tag{19}$$

where $\alpha_V$ is the volume thermal expansion coefficient and $B_0$ is the bulk modulus.

Figure 12 shows $C_V$ as a function of temperature at various pressures. $C_V$ increases dramatically as pressure increases and finally approaches $3R$.

From Eq. (19), we derived $C_P$ as a function of temperature at fixed pressures and compared the results with experimental data[32,38,54,55] in Fig. 13. Our 0-GPa results are in perfect agreement with the experiments below 200 K and diverge slightly from the experiments above 200 K, but the largest deviation is not larger than 8% in the whole temperature range.

The isothermal bulk modulus $B_T$ can be obtained from

$$B_T = \frac{1}{\alpha}\left(\frac{\partial P}{\partial T}\right)_V. \tag{20}$$

The adiabatic bulk modulus $B_S$ correlates with $B_T$ via

$$B_S - B_T = -\alpha\gamma B_T T. \tag{21}$$

Figure 14 shows the isothermal and adiabatic bulk modulus as a function of temperature and pressure. Our 0-GPa results

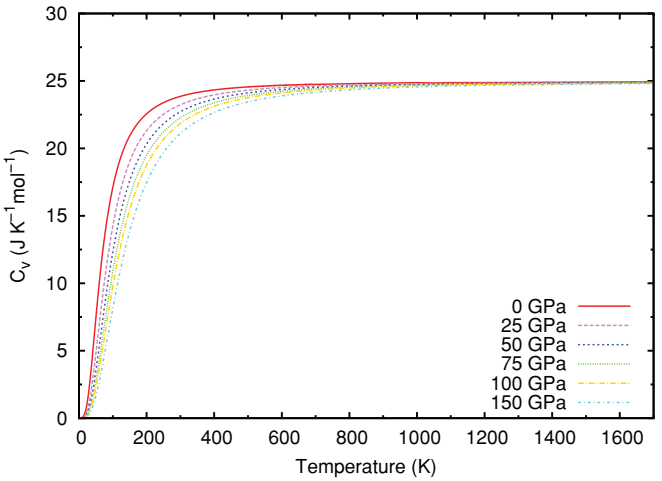


FIG. 12. (Color online) The specific heat capacity at constant volume as a function of temperature at different pressures.

for $B_T$ are consistent with experiment.[56] The two moduli both decrease with increasing temperature at fixed pressures. The temperature dependence of the two moduli becomes weaker with increasing pressure and $B_S$ is somewhat larger than $B_T$ in each set of data at the same pressure.

## IV. DISCUSSION AND CONCLUSIONS

We performed a detailed investigation on the lattice dynamics, elastic, and thermodynamic properties of Pd under pressure using DFPT and classical molecular dynamics techniques. We found that the fcc phase is stable up to 500 GPa and 5000 K compared with bcc and hcp. Using volume-conserving strains, we calculated high-pressure and high-temperature elastic constants for fcc Pd. The high-temperature results are in agreement with the available experimental data. This indicates that the contribution of the strained lattice at high temperature to the free energy is small and can be omitted for the cubic systems of Pd.

Our phonon dispersion curve at 0 GPa agrees with experiment, apart from the unobserved phonon anomalies along the

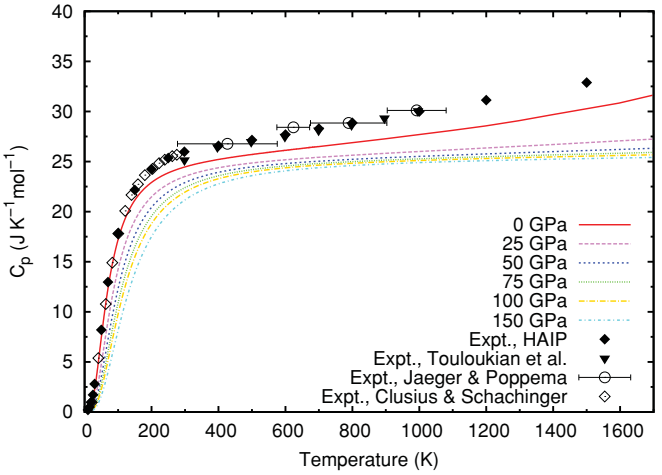


FIG. 13. (Color online) $C_P$ as a function of temperature. The experimental data are from Refs. 38, 32, 55, and 54.

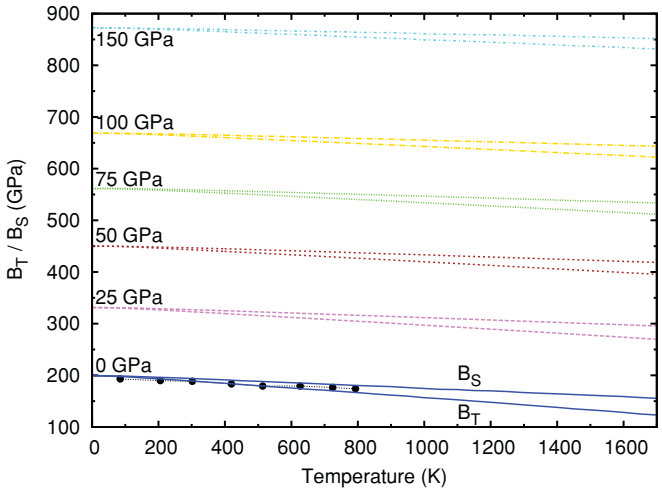


FIG. 14. (Color online) The adiabatic bulk modulus and isothermal bulk modulus vs temperature at different pressures. The solid circles are the experimental data from Ref. 56.

[110] direction in the first BZ. Based on the QHA, we deduced a wide range of thermodynamic properties for Pd, including isotherms, the thermal expansion coefficient, and Hugoniot curves. At ambient pressure, the obtained thermal expansion coefficient is in very good agreement with experiment.

We investigated the thermodynamic properties of Pd within the quasiharmonic approximation, which appears to be accurate to at least half the melting temperature, as our zero-pressure results show. At higher temperature anharmonic effects start to play a progressively important role, but these have been neglected in the present work. We also ignored the effects on the lattice dynamical properties and the change of electronic structures with increasing temperature, as well as the interactions among phonons and the interactions between electrons and phonons. The Hugoniot $P$-$V$ and $P$-$T$ curves are well reproduced up to 300 GPa, compared with the experimental data and our shock simulations. This supports the validity of the QHA for describing the shock behavior of Pd at extreme conditions. The work presented here, and in particular the systematic investigation of the EOS, is important for the use of Pd as a pressure calibrator in shock-wave and diamond-anvil-cell experiments.

## ACKNOWLEDGMENTS

We would like to acknowledge the support by the National Natural Science Foundation of China under Grant No. 11047151, the Henan Research Program of Basic and Frontier Technology under Grant No. 102300410213, and the Scientific Research Foundation of Luoyang Normal University under Grants No. 10000855 and No. 10000890.

*zl.liu@163.com

[1] F. Favier, E. C. Walter, Z. M. P., T. Benter, and R. M. Penner, Science **293**, 2227 (2001).
[2] A. Javey, J. Guo, Q. Wang, M. Lundstrom, and H. Dai, Nature (London) **424**, 654 (2003).
[3] D. A. Stewart, New J. Phys. **10**, 043025 (2008).
[4] J. M. Walsh, M. H. Rice, R. G. Mcqueen, and F. L. Yarger, Phys. Rev. **108**, 196 (1957).
[5] H. K. Mao, P. M. Bell, J. W. Shaner, and D. J. Steinberg, J. Appl. Phys. **49**, 3276 (1978).
[6] Y. Fei, J. Li, K. Hirose, W. Minarik, J. V. Orman, C. Sanloup, W. V. Westrenen, T. Komabayashi, and K. Funakoshi, Phys. Earth Planet. Inter. **143**, 515 (2004).
[7] A. Chijioke, W. J. Nellis, and I. F. Silvera, J. Appl. Phys. **98**, 073526 (2005).
[8] B. Stritzker, Phys. Rev. Lett. **42**, 1769 (1979).
[9] R. König, A. Schindler, and T. Herrmannsdörfer, Phys. Rev. Lett. **82**, 4528 (1999).
[10] T. Takezawa, H. Nagara, and N. Suzuki, Phys. Rev. B **71**, 012515 (2005).
[11] G. Y. Guo, J. Appl. Phys. **105**, 07C701 (2009).
[12] I. Y. Sklyadneva, A. Leonardo, P. M. Echenique, S. V. Eremeev, and E. V. Chulkov, J. Phys. Condens. Matter **18**, 7923 (2006).
[13] A. P. Miiller, Can. J. Phys. **53**, 2491 (1975).
[14] R. Youngblood, Y. Noda, and G. Shirane, Phys. Rev. B **19**, 6016 (1979).
[15] A. P. Miiller and B. N. Brockhouse, Phys. Rev. Lett. **20**, 798 (1968).
[16] A. P. Miiller and B. N. Brochhouse, Can. J. Phys. **49**, 704 (1971).
[17] W. Kohn, Phys. Rev. Lett. **2**, 393 (1959).
[18] S. Baroni, P. Giannozzi, and A. Testa, Phys. Rev. Lett. **58**, 1861 (1987).
[19] S. Baroni, S. D. Gironcoli, A. D. Corso, and P. Giannozzi, Rev. Mod. Phys. **73**, 515 (2001).
[20] S. Y. Savrasov and D. Y. Savrasov, Phys. Rev. B **54**, 16487 (1996).
[21] J. A. Rayne, Phys. Rev. **118**, 1545 (1960).
[22] M. Yoshihara, R. B. Mclellan, and F. R. Brotzen, Acta Metall. **35**, 775 (1987).
[23] C. Weinmann and S. Steinemann, Solid State Commun. **15**, 281 (1974).
[24] N. D. Mermin, Phys. Rev. **137**, A1441 (1965).
[25] P. Giannozzi *et al.*, J. Phys. Condens. Matter **21**, 395502 (2009).
[26] J. P. Perdew and A. Zunger, Phys. Rev. B **23**, 5048 (1981).
[27] D. Vanderbilt, Phys. Rev. B **41**, 7892 (1990).
[28] J. P. Perdew, K. Burke, and M. Ernzerhof, Phys. Rev. Lett. **77**, 3865 (1996).
[29] H. J. Monkhorst and J. D. Pack, Phys. Rev. B **13**, 5188 (1976).
[30] C. Cazorla, D. Alfè, and M. J. Gillan, Phys. Rev. B **77**, 224103 (2008).
[31] R. M. Wentzcovitch, Phys. Rev. B **44**, 2358 (1991).
[32] Y. S. Touloukian, R. K. Kirby, R. E. Taylor, and T. Y. R. Lee, *Thermophysical Properties of Matter* (Plenum, New York, 1970).
[33] F. Birch, J. Geophys. Res. **83**, 1257 (1978).
[34] F. Birch, J. Geophys. Res. **91**, 4949 (1986).
[35] Y. Wang, J. J. Wang, H. Zhang, V. R. Manga, S. L. Shang, L. Q. Chen, and Z. K. Liu, J. Phys. Condens. Matter **22**, 225404 (2010).
[36] O. Gülseren and R. E. Cohen, Phys. Rev. B **65**, 064103 (2002).

[37]S. Y. Savrasov and D. Y. Savrasov, Phys. Rev. B **46**, 12181 (1992).
[38]D. E. Gray, ed., *American Institute of Physics Handbook*, 3rd ed. (McGraw-Hill, New York, 1972).
[39]B. N. Dutta and B. Dayal, Phys. Status Solidi **3**, 2253 (1963).
[40]E. A. Owen and J. I. Jones, Proc. Phys. Soc. **49**, 587 (1937).
[41]C. Cagran and G. Pottlacher, Platinum Metals Rev. **50**, 144 (2006).
[42]Z. L. Liu, L. C. Cai, X. R. Chen, Q. Wu, and F. Q. Jing, J. Phys. Condens. Matter **21**, 095408 (2009).
[43]T. Sun, K. Umemoto, Z. Wu, J. C. Zheng, and R. M. Wentzcovitch, Phys. Rev. B **78**, 024304 (2008).
[44]S. P. Marsh, ed., *Los Alamos Shock Hugoniot Data* (University of California Press, Berkeley, 1979).
[45]M. V. Thiel, ed., Lawrence Livermore Laboratory Report UCRL-50108, 1977.
[46]R. G. McQueen, S. P. Marsh, J. W. Taylor, J. N. Fritz, and W. J. Carter, *The Equation of State of Solids from Shock Wave Studies* (Academic, New York, 1970).
[47]M. S. Daw and M. I. Baskes, Phys. Rev. B **29**, 6443 (1984).
[48]S. M. Foiles, M. I. Baskes, and M. S. Daw, Phys. Rev. B **33**, 7983 (1986).
[49]Z. L. Liu, J. H. Yang, Z. G. Zhao, L. C. Cai, and F. Q. Jing, Phys. Lett. A **374**, 1579 (2010).
[50]S. J. Plimpton, J. Comput. Phys. **117**, 1 (1995).
[51]S. J. Plimpton, R. Pollock, and M. Stevens, in *Proceedings of the Eighth SIAM Conference on Parallel Processing for Scientific Computing* (March, 1997).
[52][http://lammps.sandia.gov/index.html].
[53]Z. L. Liu, L. C. Cai, X. R. Chen, and F. Q. Jing, Phys. Rev. B **77**, 024103 (2008).
[54]K. Clusius and L. Schachinger, Z. Naturforsch. 2A, 90 (1947).
[55]F. M. Jaeger and T. J. Poppema, Recl. Trav. Chim. **55**, 492 (1936).
[56]*Landolt-Börnstein New Series*, Vol. 18 (Springer, Berlin, 1984).